

Title	Persistence of ferroelectricity close to unit-cell thickness in structurally disordered Aurivillius phases
Authors	Keeney, Lynette;Saghi, Zineb;O'Sullivan, Marita;Alaria, Jonathan;Schmidt, Michael;Colfer, Louise
Publication date	2020-12-01
Original Citation	Keeney, L., Saghi, Z., O'Sullivan, M., Alaria, J., Schmidt, M. and Colfer, L. (2020) 'Persistence of ferroelectricity close to unit-cell thickness in structurally disordered Aurivillius phases', Chemistry of Materials, 32(24), pp. 10511-10523. doi: 10.1021/acs.chemmater.0c03454
Type of publication	Article (peer-reviewed)
Link to publisher's version	10.1021/acs.chemmater.0c03454
Rights	© 2020, American Chemical Society. This document is the Accepted Manuscript version of a Published Work that appeared in final form in Chemistry of Materials, after technical editing by the publisher. To access the final edited and published work see https://doi.org/10.1021/acs.chemmater.0c03454
Download date	2025-04-24 20:27:31
Item downloaded from	https://hdl.handle.net/10468/10951



UCC

University College Cork, Ireland
Coláiste na hOllscoile Corcaigh

Supporting Information for:

Persistence of ferroelectricity close to unit-cell thickness in structurally disordered Aurivillius phases

Lynette Keeney^{1*}, Zineb Saghi², Marita O'Sullivan³, Jonathan Alaria³, Michael Schmidt¹, Louise Colfer¹

1. Tyndall National Institute, University College Cork, 'Lee Maltings', Dyke Parade, Cork, T12 R5CP, Ireland
2. Université Grenoble Alpes, CEA, LETI, Grenoble, F-38000, France.
3. Department of Physics, University of Liverpool, Liverpool, L69 7ZE, UK.

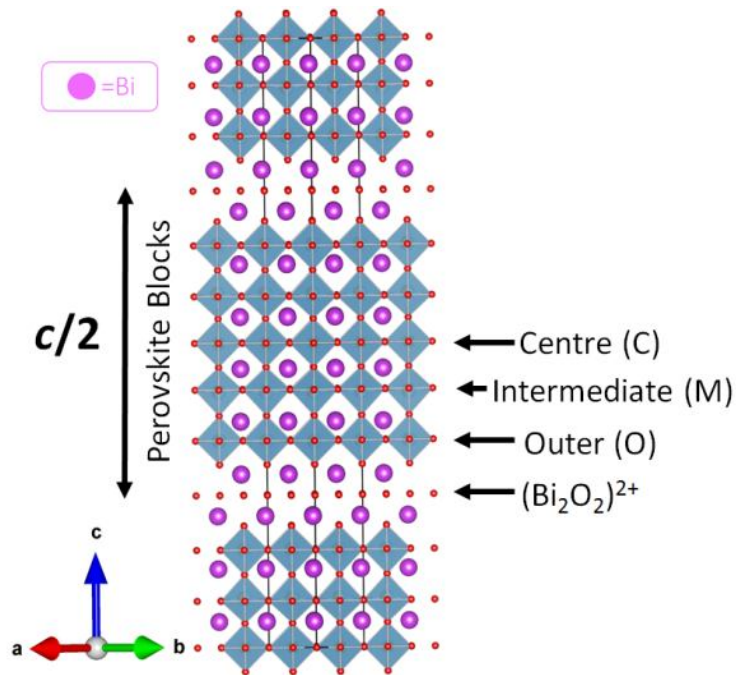


Figure S 1. Schematic of a five-layered Aurivillius phase structure, illustrating layered intergrowths of fluorite-like $(\text{Bi}_2\text{O}_2)^{2+}$ units alternating with perovskite-like units having Bi cations at the A-sites (purple) and transition metal cations at the B-sites. BO_6 octahedra are represented by blue polyhedra and oxygen atoms are displayed in red. Adapted from the original source, Fig. 1 (a) in Keeney, L. *et al.*, *Sci. Rep.*, 7, 1737 (2017)¹, to include a legend representing the bismuth atoms and a scale-bar to indicate half a unit-cell length ($c/2$). This image was used and adapted under the terms of the Creative Commons Attribution 4.0 International License (<http://creativecommons.org/licenses/by/4.0/>).

Direct evidence for partitioning of magnetic cations within the B6TFMO layered material was demonstrated previously using atomic-resolution electron microscopy.¹ Driven by strain- and electrostatic-energy factors, there is a marked preference for manganese cations to position to the center-most layer of the structure. This increases the probability of nearest neighbor magnetic interactions in the central layer by up to 90% compared to a case where the magnetic cations are randomly distributed over the 5 available B-sites. This is pivotal in explaining pathways to long-range magnetic order which are unique to the manganese-containing samples.

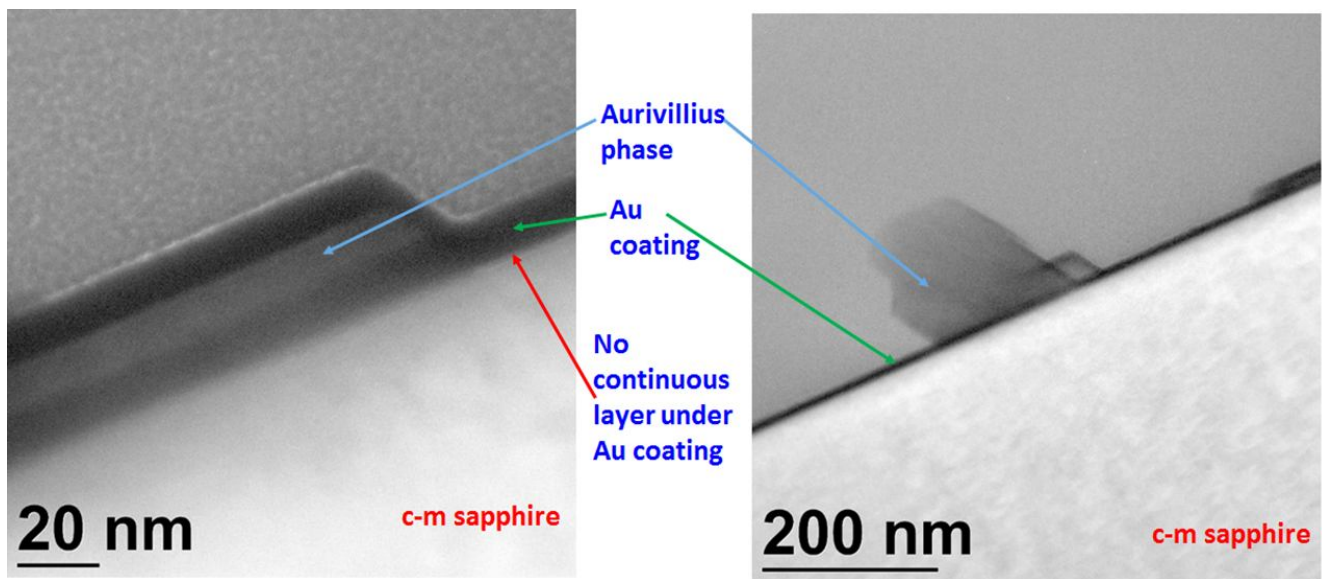


Figure S 2 (a) and (b). Representative TEM images demonstrating non-continuous growth of Aurivillius phase layers when performing DLI-CVD using 100 injections on c-m sapphire substrates.

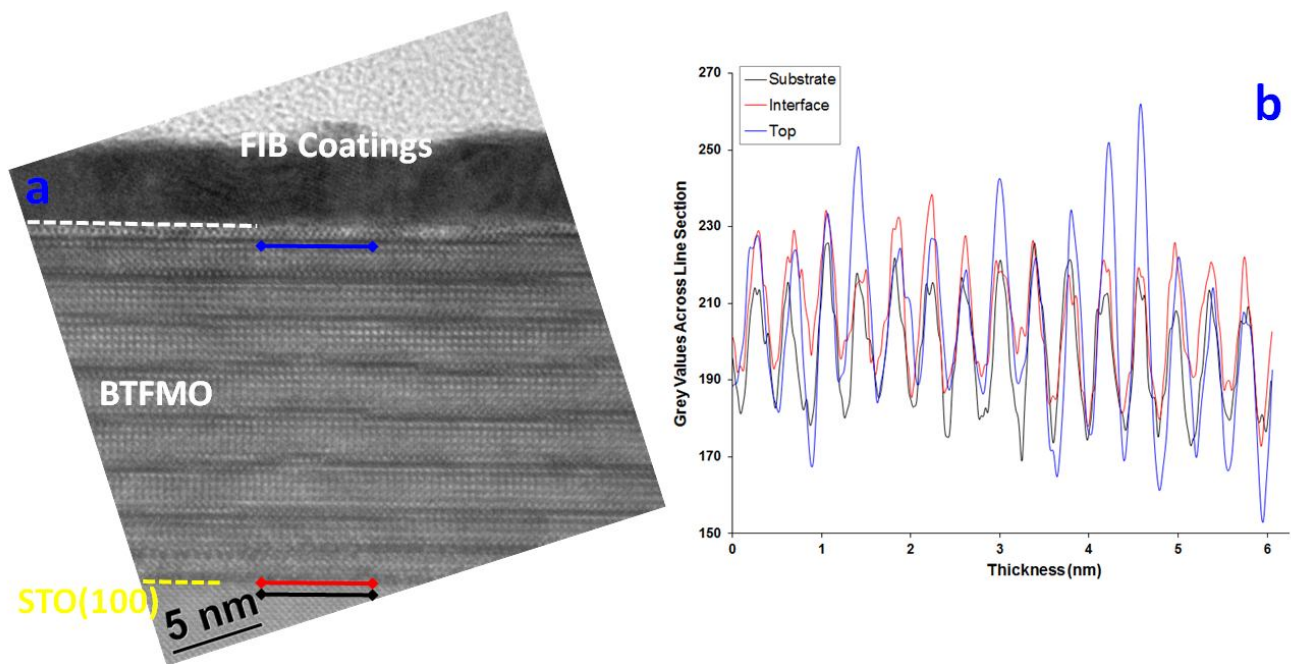


Figure S 3 (a) TEM image of 18.2 nm BTFMO on STO (100) prepared by the 2-step process (post-anneal 850 °C). Line section measurements along the [100] direction of TEM data for substrate (black line), interface (red line) and top of BTFMO film (blue line) are plotted in **(b)** and enable a comparison between lattice parameter of BTFMO film and corresponding substrate, as tabulated in **Fig. 1 (g)**.

Defects observed in BTFMO samples prepared by the 2-step process:

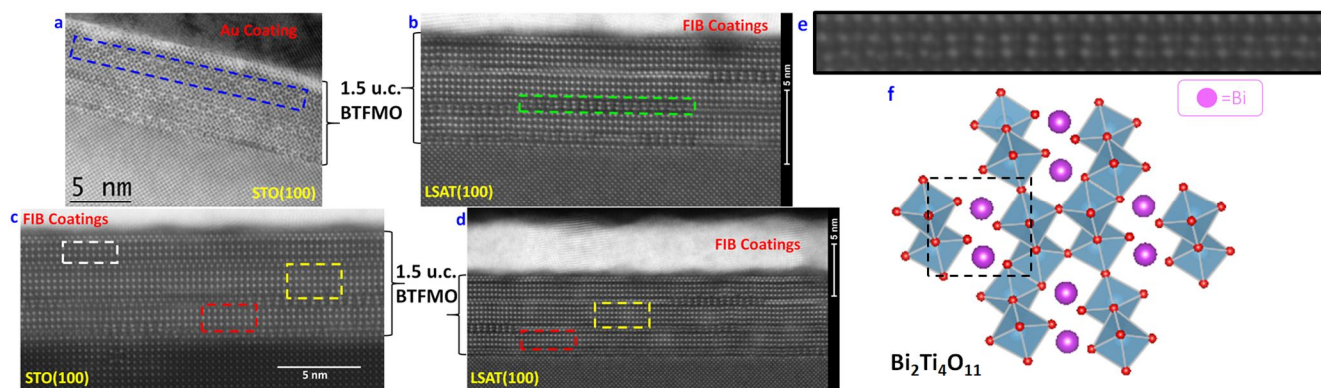


Figure S 4 (a) Conventional TEM image of BTFMO on STO (100) prepared by the 2-step process (post-anneal 850 °C). The region highlighted by the blue rectangle is representative of a defect region which is thicker (~0.6 nm) than ~0.408 nm normally expected for the $(\text{Bi}_2\text{O}_2)^{2+}$ interlayer. Aberration-corrected STEM images of BTFMO prepared by the 2-step process demonstrate that these bismuth-poor interfaces are based on anatase-like chains of edge-sharing BO_6 octahedra which create “S-shaped tunnels”, stabilized by double columns of Bi^{3+} cations, highlighted by the green rectangle in (b) and also evident in (c), (d) along with intergrowth regions of $m = 3$ (representative area shown in white rectangle), $m = 4$ (representative area shown in red rectangle) together with the $m = 5$ (representative area shown in yellow rectangle) Aurivillius-type phases. (e) An enlarged image of the anatase-like chains. As Batuk *et al.*² describe, these defect regions can be considered as intergrowths between the perovskite blocks and polysynthetically twinned fragments of the $\text{Bi}_2\text{Ti}_4\text{O}_{11}$ structure. (f) Schematic of the crystal structure of $\text{Bi}_2\text{Ti}_4\text{O}_{11}$ (JCPDS 72-1820³) drawn using VESTA⁴ software. Bismuth cations are represented by purple spheres, oxygen cations are represented by red spheres and titanium cations are represented by blue polyhedra. An “S-shaped tunnel”, similar to that observed within the bismuth-poor defect regions in BTFMO, is highlighted by the black rectangle.

A common defect occurring in materials of high structural anisotropy, such as the Aurivillius phases, are out-of-phase boundary (OPB) defects. These are boundary defects characterized by displacement by a fraction of a lattice parameter (c/x) between two neighboring regions parallel to the z-direction. These appear as ‘steps’ as viewed edge-on in HAADF-STEM images in reference 1.¹

Interestingly, another type of unique defect associated with volatilization of bismuth is revealed for the BTFMO films (prepared by the 2-step process involving post-anneal at 850°C) and is more abundant within these films compared to the typical OPBs associated with Aurivillius samples. In the conventional TEM images (Fig. S 4 (a)), it appears that the regions where the fluorite-like $[\text{Bi}_2\text{O}_2]^{2+}$ interlayers normally reside are thicker (~0.6 nm) than the ~0.408 nm determined by Lomanova *et al.*⁵ On closer examination using probe-corrected high resolution HAADF-STEM imaging (Fig. S 4 (b)-(e)), it is evident that these are not in fact typical fluorite-type layers. Rather, these bismuth-poor interfaces are based on anatase-like chains of edge-sharing BO_6 octahedra, similar to the periodic interfaces which separate the perovskite blocks in the recently-discovered family of layered perovskites, $\text{Bi}_{3n+1}\text{Ti}_7\text{Fe}_{3n-3}\text{O}_{9n+11}$, reported by Batuk *et al.*,^{2,6} the planar (Ti-rich) and stepped (Fe-rich) defects observed for the Ti and Nd codoped bismuth ferrite $(\text{Bi}_{0.85}\text{Nd}_{0.15})(\text{Ti}_{0.1}\text{Fe}_{0.9})\text{O}_3$ ceramics reported by MacLaren *et al.*^{7,8} and at the heterointerfaces of the $\text{PbTiO}_3/\text{BiFeO}_3$ bilayers reported by Liu *et al.*⁹ The homologous series $\text{Bi}_{3n+1}\text{Ti}_7\text{Fe}_{3n-3}\text{O}_{9n+11}$ is described as being comprised of intergrowths of the 2D perovskite and 1D anatase fragments, or can be considered as intergrowths of perovskite modules and polysynthetically twinned modules of the monoclinic $\text{Bi}_2\text{Ti}_4\text{O}_{11}$ structure (Fig. S 4 (f)).^{2,6} The anatase-like chains, together with the octahedra of the perovskite blocks create “S-shaped tunnels”, which are occupied by and stabilized by double columns of lone pair, stereochemically active Bi^{3+} cations. The double Bi columns at the interfaces create a “zig-zag” pattern of Bi atoms between the perovskite blocks (Fig. S 4 (e)).⁶ The anatase-like interfaces can be laterally shifted with respect to each other over $\pm 1/3a$,² introducing an additional degree of disorder and complexity alongside the vertical displacements associated with OPBs. To the best of our knowledge, the occurrence of this type of defect within the Aurivillius phases has not yet been previously described in the literature, it is likely that these anatase-type defects occur in other epitaxial Aurivillius phases¹⁰. We remark that our awareness and understanding of novel defect structures increases with advances in electron microscopy instrumentation.^{7,8,11}

Stacking faults and intergrowths of differing ‘m’ numbers also accompany the stepped defects at the anatase-type interfaces. Here, the physical disruption of the Aurivillius phase lattice associated with shifts of the interfaces relative to each other can be accompanied by an insertion or deletion of perovskite layers within the perovskite block. Particularly when utilizing a post-growth anneal at 850 °C, bismuth migration and out-diffusion through epitaxial BTFMO films on STO and LSAT leads to changes to local stoichiometry and results in a substantial presence of stacking fault regions due to intergrowths of $m = 3$ (representative area shown in white rectangle) and $m = 4$ (representative area shown in red rectangle) phases together with the $m = 5$ (representative area shown in yellow rectangle) Aurivillius-type phase, as observed in the STEM images (Fig. S 4 (c), (d)).

It is interesting to consider the effects that these defects may have on the physical properties of the BTFMO thin films. Previous work on B6TFMO demonstrates that disruptions of the Aurivillius phase lattice by OPB defects results in increased partitioning of magnetic cations to the inner perovskite layers of B6TFMO.¹ Cation ordering is also noted in the vicinity of the anatase-type interfaces of the $\text{Bi}_{3n+1}\text{Ti}_7\text{Fe}_{3n-3}\text{O}_{9n+11}$ system reported by Batuk *et al.*,^{2,6} which require *B*-site cations with higher formal charge (e.g. Ti^{4+}) to compensate for the bismuth cation deficiency at the interfaces. The Ti tends to concentrate to the center of the anatase-like interfaces, whereas the Fe-atoms are predominantly found in the adjacent perovskite blocks.^{2,6} The core of the anatase-type chains is reported to have excess negative charge, which results in a strong polarization of the surrounding perovskite and the stabilization of a polar phase in the immediate vicinity of the defect, in preference to the antiferroelectric matrix of the $\text{Bi}_{3n+1}\text{Ti}_7\text{Fe}_{3n-3}\text{O}_{9n+11}$ system.^{2,6} Although atomic resolution chemical mapping at the anatase-type defect regions has not been performed as part of this study, it is possible that these anatase-type defects could also locally influence the magnetic cation ordering and strength of the ferroelectric polarization within the BTFMO films. This will be explored in future work.

Overall however, in the case of the BTFMO films prepared by the 2-step process involving post-anneal at 850°C, bismuth volatilization has a detrimental effect on the quality of the films and assists in the formation of impurity phases.

Impurity phases observed in BTFMO samples prepared by the 2-step process:

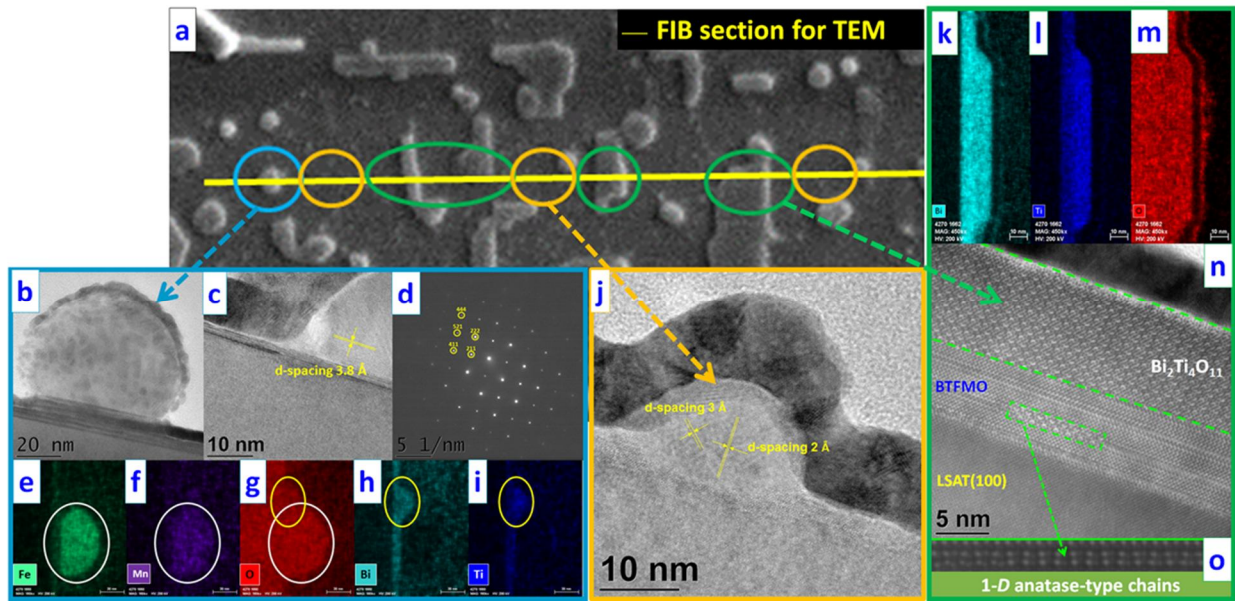


Figure S 5 (a) SEM image of BTFMO on LSAT (100) prepared by the 2-step process (post-anneal 850 °C). The yellow line represents the FIB path used to prepare a cross-section of the sample for TEM analysis. (b), (c) TEM images, (d) electron diffraction pattern and (e)-(g) regions encircled by the white oval in STEM-EDX images demonstrate that this impurity is of the bixbyite $(\text{Mn,Fe})_2\text{O}_3$ (cubic Ia-3) phase (large spherical structure). The region highlighted by the yellow oval in (g)-(i) is an amorphous phase with the $\text{Bi}_x\text{Ti}_y\text{O}_z$ composition. (j) TEM image of the spinel $(\text{Mn,Fe})_3\text{O}_4$ (cubic space group Fd-3m) impurity phase (smaller ‘speckle’). (k)-(m) STEM-EDX images and (n) representative TEM image of the monoclinic $\text{Bi}_2\text{Ti}_4\text{O}_{11}$ (B2/b) titanium-rich impurity phase (structure parallel with the (100) surface orientation). 1-D anatase-type chains are present within the underlying BTFMO film as observed (n) within the green rectangle of the conventional TEM image and when focusing into (o) a portion of an aberration-corrected STEM image.

The following impurity precipitates have been identified by TEM imaging, including: i) relatively large (> 40 nm diameter) circular structures (**Fig. S 5** (b) – (g)), sometimes having a ii) smaller (approx. 30 nm, amorphous) structure adjacent to them (**Fig. S 5** (g)-(i)), iii) relatively smaller (< 20 nm diameter) “speckles” (**Fig. S 5** (j)), and iv) plate-type structures parallel with the (100) surface orientation (**Fig. S 5** (k)-(o)). STEM-EDX of the white regions encircled in **Fig. S 5** (e) – (g) demonstrates that the larger circular structures i) within the encircled blue region in **Fig. S 5** (a) are oxides containing manganese and iron. HR-TEM (**Fig. S 5** (b) – (c)) and selected area electron diffraction (SAED) patterns (**Fig. S 5** (d)) demonstrate that this structure corresponds with the bixbyite $(\text{Mn,Fe})_2\text{O}_3$ (cubic Ia-3) phase (3.8 Å, 2.7 Å, 2.2 Å, 1.7 Å and 1.3 Å correspond with the (211), (222), (411), (521), (444) reflections, respectively), which tends to form above 805 °C.^{12,13} It should be noted that the SAED images have an error bar of ± 5%. The adjacent amorphous phase ii) encircled in yellow in **Fig. S 5** (g)-(i) is of the $\text{Bi}_x\text{Ti}_y\text{O}_z$ composition. HR-TEM analysis indicate that the speckles iii) encircled in orange in **Fig. S 5** (a) have the spinel $(\text{Mn,Fe})_3\text{O}_4$ (cubic space group Fd-3m) structure as indicated by the 3.0 Å and 2.1 Å d-spacings corresponding to the (220) and (400) reflections, respectively (**Fig. S 5** (j)), which can crystallize at 350 °C.^{12,14}

Elemental analysis (**Fig. S 5 (k) - (m)**) of the plate-type structures iv) encircled in green in **Fig. S 5 (a)** demonstrates that these are mainly composed of Bi, Ti and O and are titanium rich, having > 22 atom% higher titanium content compared with the underlying Aurivillius phase film. TEM imaging (**Fig. S 5 (n)**) indicates that this is the monoclinic $\text{Bi}_2\text{Ti}_4\text{O}_{11}$ (B2/b) phase consisting of double chains of TiO_6 -type octahedra interlinked to form channels where the double columns of Bi^{3+} cations are accommodated.^{2,3,15} Similarities are noted between the 1-D anatase-like intergrowths discussed above, which create the ‘S-shaped’ Bi^{3+} accommodating tunnels within the underlying Aurivillius film (**Fig. S 5 (n) – (o)**). $\text{Bi}_2\text{Ti}_4\text{O}_{11}$ ceramics are reported to be antiferroelectric¹⁵ and tend to form above 800 °C.^{16,17}

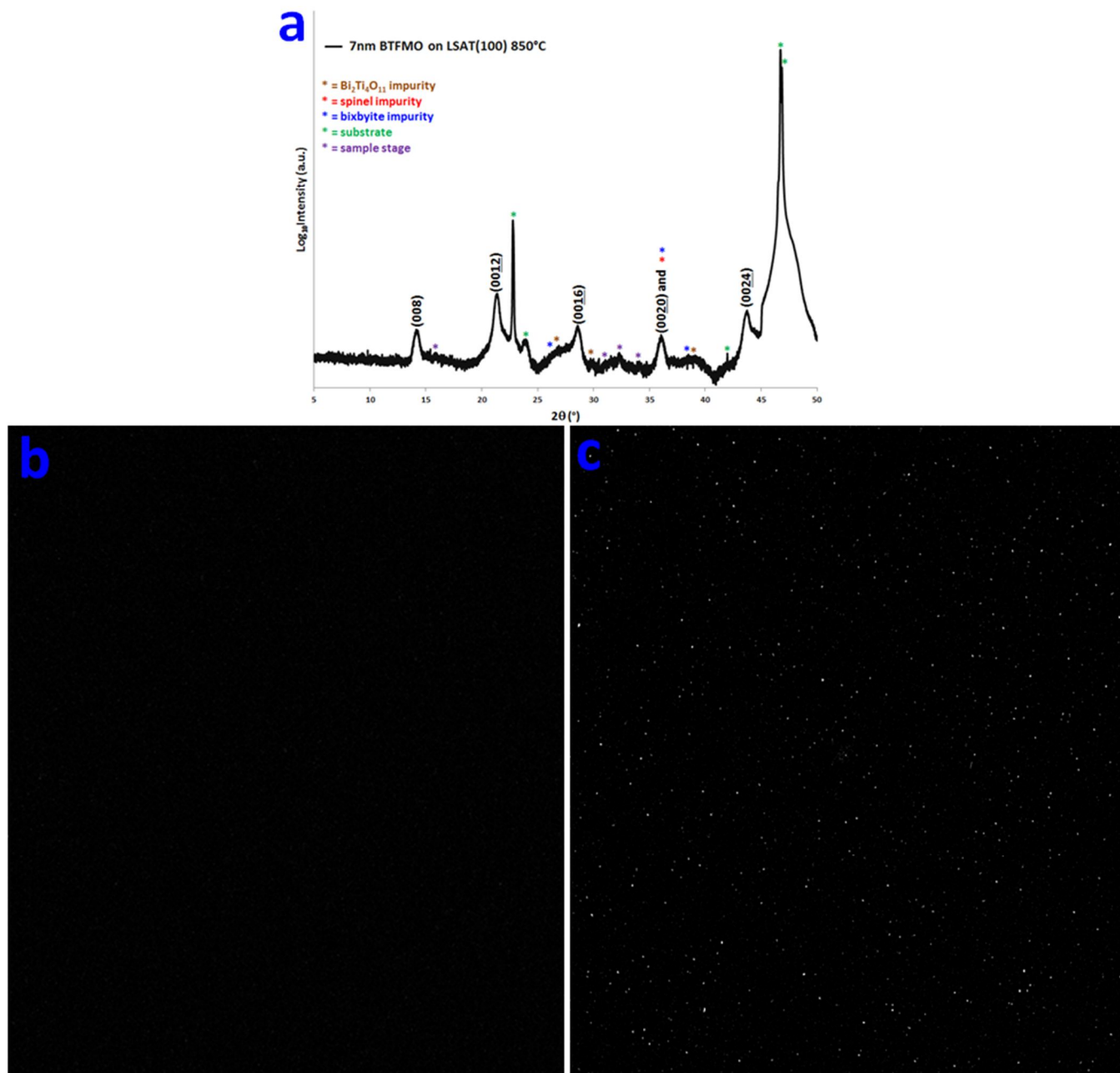


Figure S 6 (a) XRD pattern of 7 nm BTFMO on LSAT(100) prepared by the 2-step process (post-anneal 850 °C). Compositional maps of thicker (~ 100 nm) BTFMO films prepared by the 2-step process on **(b)** c-m plane sapphire and **(c)** STO (100). These were produced by extended period (72 h) SEM-EDX data collections from a 100 μm^2 sample area, followed by subtraction of the $\text{BiL}\alpha$ from the $\text{FeK}\alpha$ signal. The white ‘flecks’ in **(c)** correspond to Fe-rich areas where the Fe content exceeds the surrounding grains of the main Aurivillius phase. These Fe-rich areas are not observed in **(b)**, implying that these surface impurities are characteristic of films grown on epitaxial substrates only.

XRD Peak Broadening in B6TFMO films prepared by the 2-step process:

The diffraction peaks are collected from X-rays that coherently scatter through only 1 or 1.5 u.c. with grains having relatively small dimensions (<20 nm) and peak broadening is observed in the XRD patterns (e.g. full width of half maxima are (0010) = 1.152°, (0022) = 1.218° and (0024) = 1.185° (**Fig. 2 (c)**; 710 °C); (0010) = 1.215°, (0022) = 1.189° and (0024) = 1.166° (**Fig. 2 (e)**; 700 °C) and (0010) = 1.669°, (0020) = 2.200° and (0022) = 2.003° (**Fig. 3 (e)**)). Peak broadening may also be attributed to a disordered sample having perovskite layers of varying thickness, as observed in TEM images (**Fig. S 7**).

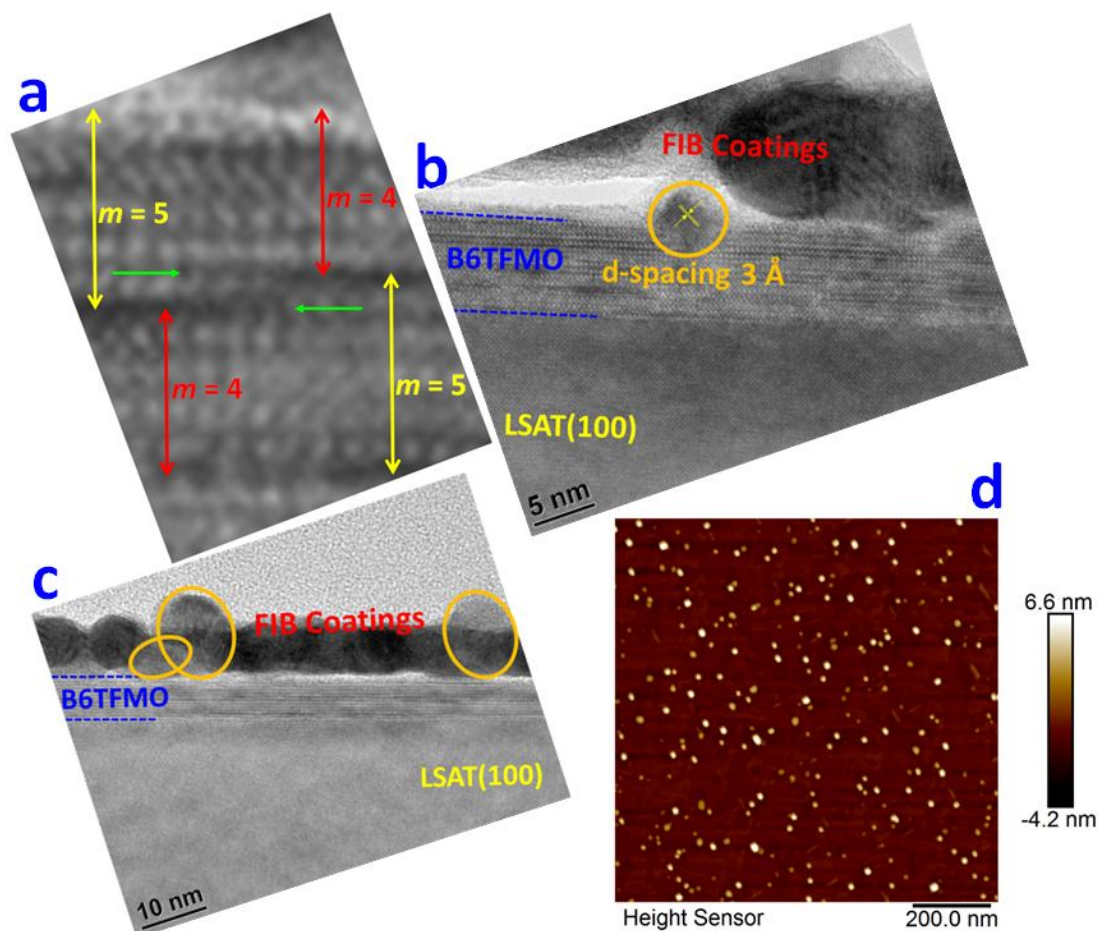


Figure S 7 (a) Enlarged portion of a TEM image of 7 nm B6TFMO prepared by the single-step DLI-CVD process (700 °C) on LSAT (100). Whereas the majority of the sample is comprised of the $m = 5$ Aurivillius phase, occasional changes in the thickness of the perovskite blocks are observed at specific regions accompanying OPB defects (within the green arrows) where stacking faults of $m = 4$ phases form. TEM images of (b) 7 nm and (c) 5 nm B6TFMO prepared by the single-step DLI-CVD process (700 °C) on LSAT (100) confirm the presence of impurity ‘speckles’ both (b) within and (c) on the surface of the Aurivillius phase film. d -spacings of 3.0 Å and 2.1 Å are observed corresponding to the (220) and (400) reflections spinel $(\text{Mn,Fe})_3\text{O}_4$ (cubic space group $\text{Fd-}3\text{m}$) phase. (d) Representative AFM image of 7 nm B6TFMO prepared by the single-step DLI-CVD process (710 °C) on LSAT (100) demonstrating these ‘island’-type impurities present on the surface at a volume fraction of 3-4 vol. %.

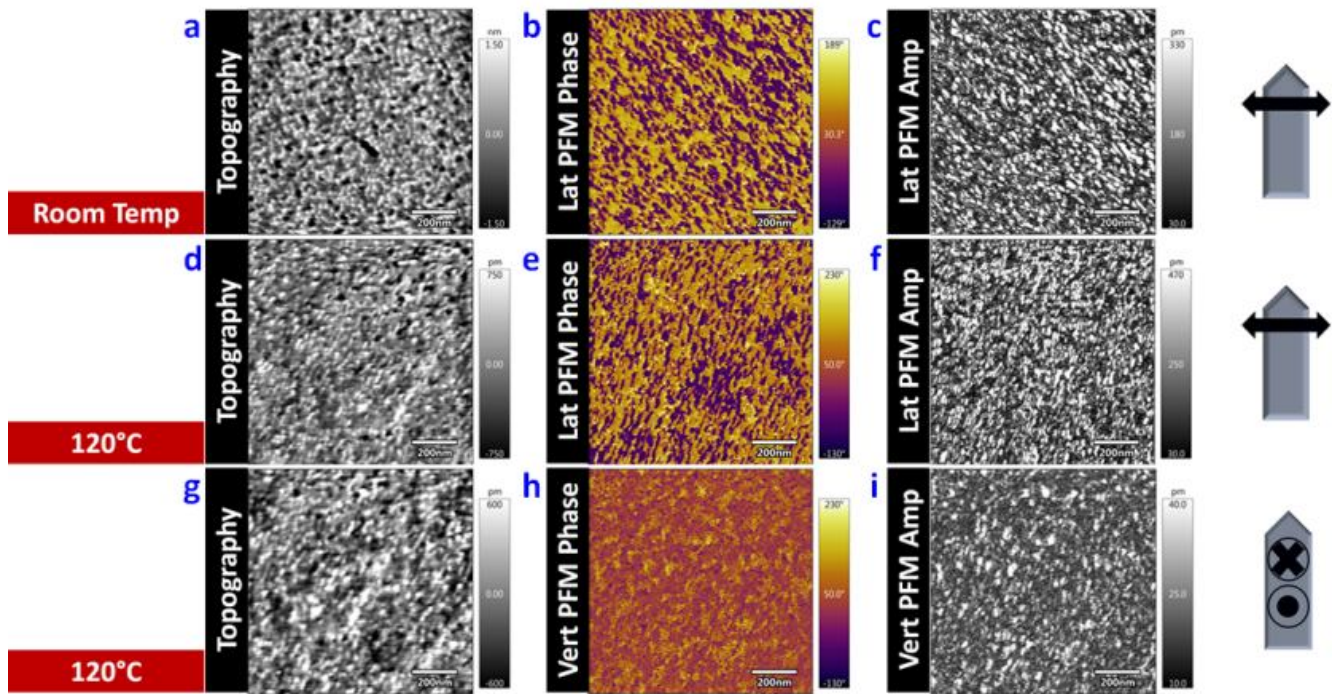


Figure S 8. DART-PFM images of 7 nm B6TFMO on NGO (001) prepared by the 1-step process (710 °C). (a), (b), (c) Room temperature topography, lateral (lat) PFM phase and lateral PFM amplitude (amp) images, respectively. (d), (e), (f) Topography, lateral PFM phase and lateral PFM amplitude images, respectively, where the B6TFMO sample was maintained at 120 °C. (g), (h), (i) Topography, vertical (vert) PFM phase and vertical PFM amplitude images, respectively, where the B6TFMO sample was maintained at 120 °C. The direction of motion of the PFM cantilever as it scans the sample surface is indicated to the right of the images. These studies demonstrate the persistence of ferroelectricity at 1.5 u.c. B6TFMO.

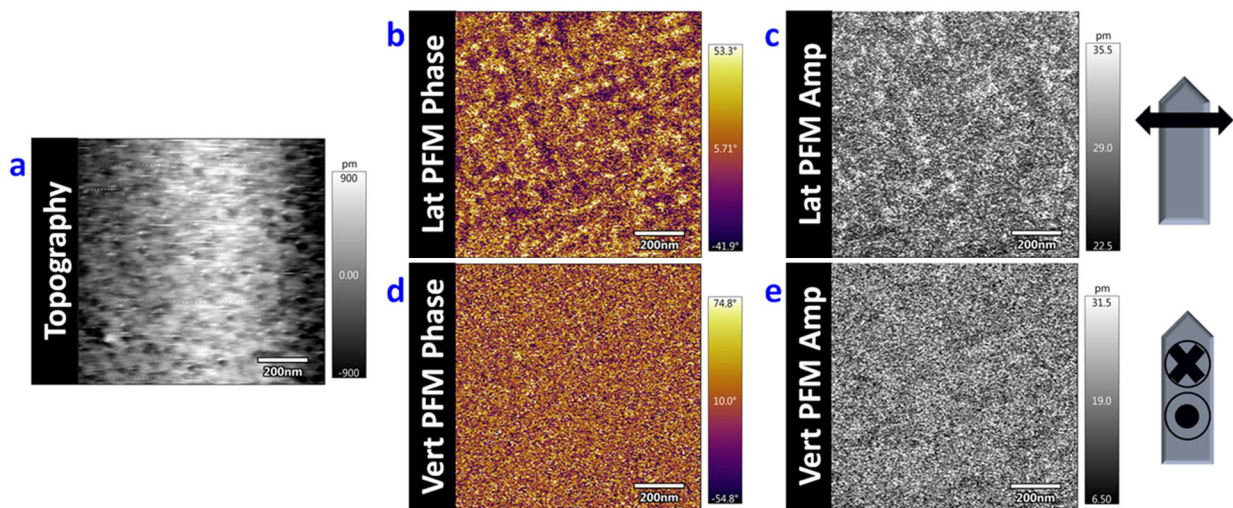


Figure S 9. Representative single frequency (15 kHz) PFM images of 5 nm (1. u.c.) B6TFMO on NGO (001) prepared by the 1-step process (700 °C). Room temperature (a) topography, (b) lateral (lat) PFM phase, (c) lateral PFM amplitude (amp) images, (d) vertical (vert) PFM phase and (e) vertical PFM amplitude images. The direction of motion of the PFM cantilever as it scans the sample surface is indicated to the right of the images. As the probing signal (V_{AC}) is driven at a single frequency (15 kHz; below the contact resonance of the cantilever) this technique enables measurements of piezoresponse, however the signal to noise ratio is not amplified by resonance enhancement.

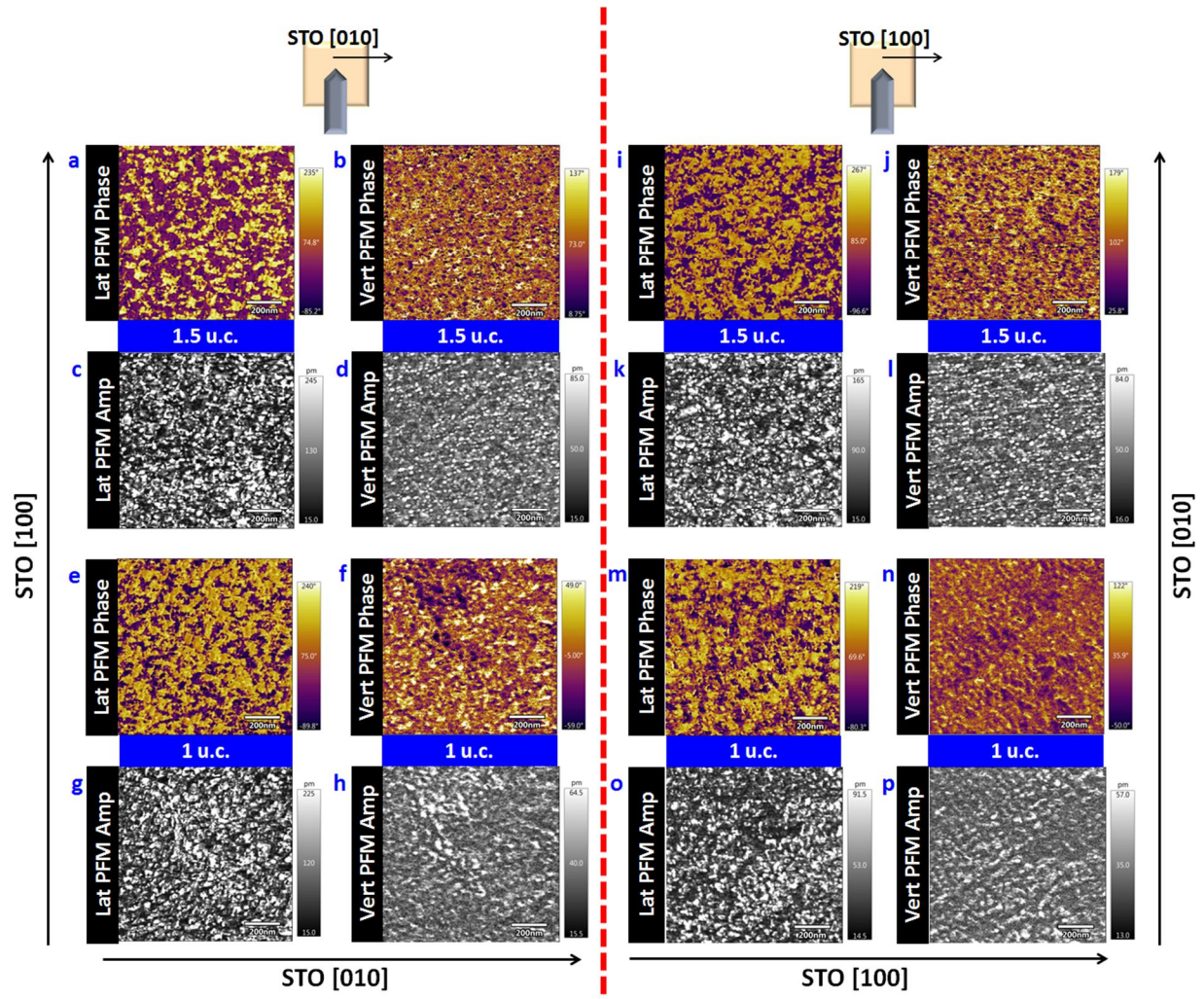


Figure S 10. Lateral (lat) and vertical (vert) DART-PFM phase and amplitude (amp) images of B6TFMO films on STO (100) with thickness of 7 nm (1.5 u.c.) and 5 nm (1 u.c.) obtained using a “super sharp” probe (<5 nm tip radius). Images (a) to (h) were performed with the cantilever scanning direction parallel to the $[010]_{\text{STO}}$ axis. The samples were rotated 90° for images (i) to (p) where the cantilever scanning direction was parallel to the $[100]_{\text{STO}}$ axis. These images demonstrate the isotropic random distribution of in-plane and out-of-plane domains at 1.5 and 1 unit cell thicknesses for B6TFMO on STO (100). Uniaxial ferroelectric anisotropy is not observed at 1.5 and 1 unit cell thicknesses.

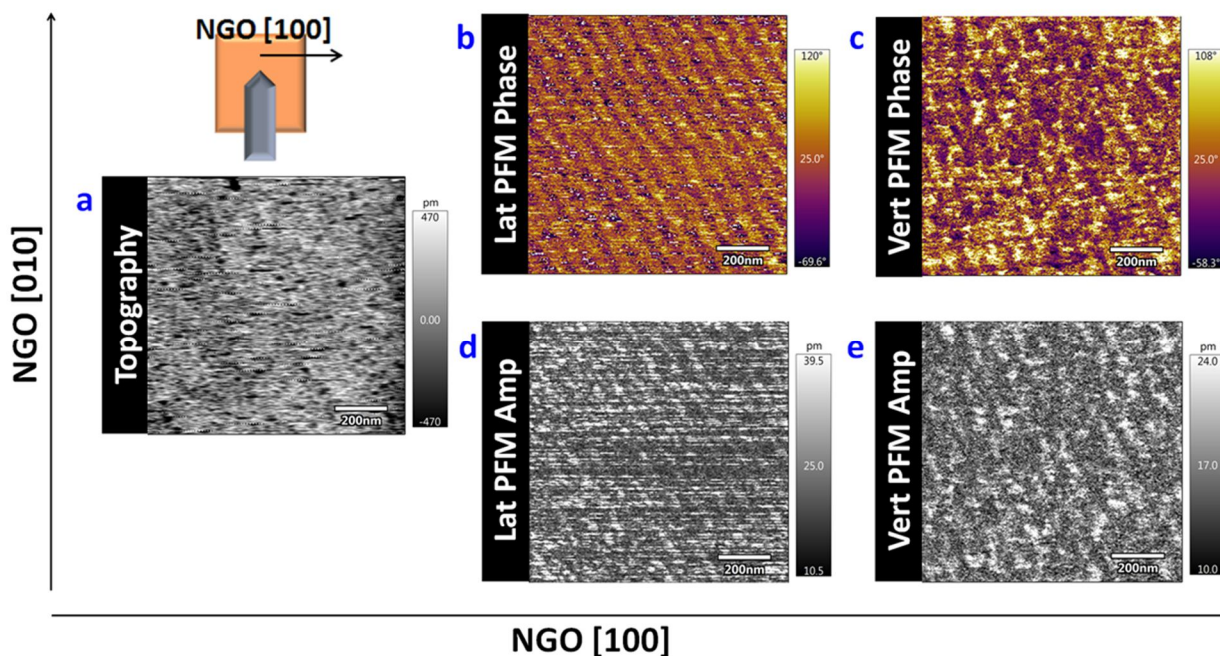


Figure S 11. (a) Topography, (b), (d) lateral (lat) and (c), (e) vertical (vert) DART-PFM phase and amplitude (amp) images of 5 nm thick (1 u.c.) B6TFMO films on NGO (100) obtained using a “super sharp” probe (<5 nm tip radius). These studies indicate that domains are oriented 45° away from the Aurivillius phase polar axis ([010]_{NGO}).

References:

- (1) Keeney, L.; Downing, C.; Schmidt, M.; Pemble, M. E.; Nicolosi, V.; Whatmore, R. W. Direct atomic scale determination of magnetic ion partition in a room temperature multiferroic material. *Scientific Reports* **2017**, *7*, 1737.
- (2) Batuk, D.; Tsirlin, A. A.; Filimonov, D. S.; Zakharov, K. V.; Volkova, O. S.; Vasiliev, A.; Hadermann, J.; Abakumov, A. M. Bi_{3n+1}Ti₇Fe_{3n-3}O_{9n+11} Homologous Series: Slicing Perovskite Structure with Planar Interfaces Containing Anatase-like Chains. *Inorganic Chemistry* **2016**, *55*, 1245-1257.
- (3) Petushkova, L. V.; Dmitrieva, S. P.; Pobedimskaya, E. A.; Belov, N. B. Crystalline structure of Bi₂Ti₄O₁₁. *Doklady Akademii Nauk SSSR* **1974**, *216*, 544-546.
- (4) Momma, K.; Izumi, F. VESTA 3 for three-dimensional visualization of crystal, volumetric and morphology data. *J. Appl. Cryst.* **2011**, *44*, 1272-1276.
- (5) Lomanova, N. A.; Morozov, M. I.; Ugolkov, V. L.; Gusarov, V. V. Properties of aurivillius phases in the Bi₄Ti₃O₁₂-BiFeO₃ system. *Inorganic Materials* **2006**, *42*, 189-195.
- (6) Batuk, D.; Batuk, M.; Filimonov, D. S.; Zakharov, K. V.; Volkova, O. S.; Vasiliev, A. N.; Tyablikov, O. A.; Hadermann, J.; Abakumov, A. M. Crystal Structure, Defects, Magnetic and Dielectric Properties of the Layered Bi_{3n+1}Ti₇Fe_{3n-3}O_{9n+11} Perovskite-Anatase Intergrowths. *Inorganic Chemistry* **2017**, *56*, 931-942.
- (7) MacLaren, I.; Wang, L.; Craven, A. J.; Ramasse, Q. M.; Schaffer, B.; Kalantari, K.; Reaney, I. M. The atomic structure and chemistry of Fe-rich steps on antiphase boundaries in Ti-doped Bi_{0.9}Nd_{0.15}FeO₃. *APL Materials* **2014**, *2*, 066106.
- (8) MacLaren, I.; Wang, L.; Morris, O.; Craven, A. J.; Stamps, R. L.; Schaffer, B.; Ramasse, Q. M.; Miao, S.; Kalantari, K.; Sterianou, I.; Reaney, I. M. Local stabilisation of polar order at charged antiphase boundaries in antiferroelectric (Bi_{0.85}Nd_{0.15})(Ti_{0.1}Fe_{0.9})O₃. *APL Materials* **2013**, *1*, 021102.
- (9) Liu, Y.; Zhu, Y.-L.; Tang, Y.-L.; Wang, Y.-J.; Li, S.; Zhang, S.-R.; Han, M.-J.; Ma, J.-Y.; Suriyaprakash, J.; Ma, X.-L. Controlled Growth and Atomic-Scale Mapping of Charged Heterointerfaces in PbTiO₃/BiFeO₃ Bilayers. *ACS Applied Materials & Interfaces* **2017**, *9*, 25578-25586.
- (10) Campanini, M.; Trassin, M.; Ederer, C.; Erni, R.; Rossell, M. D. Buried In-Plane Ferroelectric Domains in Fe-Doped Single-Crystalline Aurivillius Thin Films. *ACS Applied Electronic Materials* **2019**, *1*, 1019-1028.
- (11) Wang, L. Q.; Schaffer, B.; MacLaren, I.; Miao, S.; Craven, A. J.; Reaney, I. M. Atomic scale structure and chemistry of anti-phase boundaries in (Bi_{0.85}Nd_{0.15})(Fe_{0.9}Ti_{0.1})O₃ceramics. *Journal of Physics: Conference Series* **2012**, *371*, 012036.
- (12) Lick, I. D.; Soria, D. B. In *Tilte2009*.
- (13) Fleischer, M.; Richmond, W. E. The manganese oxide minerals, a preliminary report. *Economic Geology* **1943**, *38*, 269-286.
- (14) Fleet, M. E. The structure of magnetite: Symmetry of cubic spinels. *Journal of Solid State Chemistry* **1986**, *62*, 75-82.
- (15) Liu, J.; Duan, C.-G.; Yin, W.-G.; Mei, W. N.; Smith, R. W.; Hardy, J. R. Dielectric permittivity and electric modulus in Bi₂Ti₄O₁₁. *The Journal of Chemical Physics* **2003**, *119*, 2812-2819.
- (16) Akimov, A. I.; Savchuk, G. K. Synthesis and Sintering of Bi₂Ti₄O₁₁. *Inorganic Materials* **2004**, *40*, 716-720.
- (17) Kidchob, T.; Malfatti, L.; Marongiu, D.; Enzo, S.; Innocenzi, P. Sol-Gel Processing of Bi₂Ti₂O₇ and Bi₂Ti₄O₁₁ Films with Photocatalytic Activity. *Journal of the American Ceramic Society* **2010**, *93*, 2897-2902.